

This is an Open Access document downloaded from ORCA, Cardiff University's institutional repository: <https://orca.cardiff.ac.uk/id/eprint/102554/>

This is the author's version of a work that was submitted to / accepted for publication.

Citation for final published version:

Kwawu, Caroline R., Tia, Richard, Adei, Evans, Dzade, Nelson Y., Catlow, Charles Richard A. and De Leeuw, Nora 2017. CO₂ activation and dissociation on the low miller index surfaces of pure and Ni-coated iron metal: a DFT study. *Physical Chemistry Chemical Physics* 19 (29) , pp. 19478-19486. 10.1039/C7CP03466K

Publishers page: <http://dx.doi.org/10.1039/C7CP03466K>

Please note:

Changes made as a result of publishing processes such as copy-editing, formatting and page numbers may not be reflected in this version. For the definitive version of this publication, please refer to the published source. You are advised to consult the publisher's version if you wish to cite this paper.

This version is being made available in accordance with publisher policies. See <http://orca.cf.ac.uk/policies.html> for usage policies. Copyright and moral rights for publications made available in ORCA are retained by the copyright holders.



CO₂ activation and dissociation on the low miller index surfaces of pure and Ni-coated iron metal: a DFT study

Caroline R. Kwawu¹, Richard Tia¹, Evans Adei¹, Nelson Y. Dzade^{2*}, C. Richard A. Catlow³ and Nora H. de Leeuw^{2, 3*}

¹Department of Chemistry, Kwame Nkrumah University of Science and Technology, Kumasi, Ghana

²Department of Earth Sciences, Utrecht University, Princetonplein 9, 3584 CC, Utrecht, The Netherlands

³School of Chemistry, Cardiff University, Main Building, Park Pl, Cardiff CF10 3AT, UK

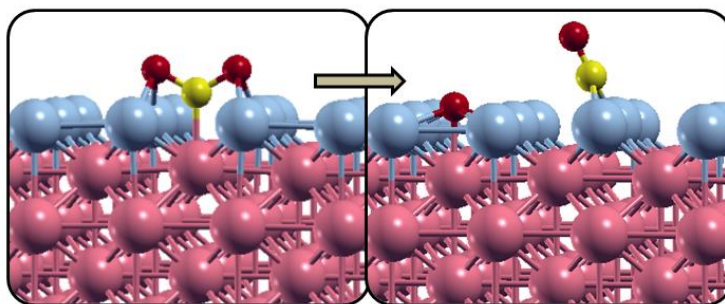
E-mail: N.Y.Dzade@uu.nl (N.Y.D); deLeeuwN@cardiff.ac.uk (N.H.dL)

Abstract

We have used spin polarized density functional theory calculations to perform extensive mechanistic studies of CO₂ dissociation into CO and O on the clean Fe (100), (110) and (111) surfaces and on the same surfaces coated by a monolayer of nickel. CO₂ chemisorbs on all three bare facets and binds more strongly to the stepped (111) surface than on the open flat (100) and close-packed (110) surfaces, with adsorption energies of -88.7 kJmol⁻¹, -70.8 kJmol⁻¹ and -116.8 kJmol⁻¹ on the (100), (110) and (111) facets, respectively. Compared to the bare Fe surfaces, we found weaker binding of the CO₂ molecules on the Ni-deposited surfaces, where the adsorption energies are calculated at +47.2 kJmol⁻¹, -29.5 kJmol⁻¹ and -65.0 kJmol⁻¹ on the Ni-deposited (100), (110) and (111) facets respectively. We have also investigated the thermodynamics and activation energies for CO₂ dissociation into CO and O on the bare and Ni-deposited surfaces. Generally, we found that the dissociative adsorption states are thermodynamically preferred over molecular adsorption, with the dissociation most favoured thermodynamically on the close-packed (110) facet. The trends in activation energy barriers were observed to follow that of the trends in surface work functions; consequently, the increased surface work functions observed on the Ni-deposited surfaces resulted in increased dissociation barriers and vice versa. These results suggest that measures to lower the surface work function will kinetically promote the dissociation of CO₂ to CO and O, although the instability of the activated CO₂ on the Ni-covered

surfaces will probably result in CO₂ desorption from the nickel-doped iron surfaces, as is also seen on the Fe(110) surface.

Graphical abstract



1. Introduction

CO₂ conversion is desirable as it can provide a source of renewable fuels and other carbon-based products that are currently obtained from fossil fuels. However, CO₂ reduction to useful hydrocarbons is still industrially challenging and its use in technological processes is therefore limited. The challenges and prospects of CO₂ conversion have been reviewed extensively¹⁻⁶. Even though CO₂ conversion under sustainable conditions is still a challenge,⁶ it is known to be converted under ambient conditions in biological systems, e.g. carbon-monoxide dehydrogenases enzymes containing Fe and Ni active sites⁸.

Single crystal heterogeneous transition metal catalysts have received much attention for potential CO₂ conversion. From the early 1980s onwards, several experimental studies have been undertaken to understand the behavior of CO₂ on transition metal surfaces; these studies have been compiled in two reviews^{9, 10}. In general, except for a few late transition metals such as Fe, Ni, and Cu, CO₂ was found not to be activated on clean transition metal surfaces, except when

promoted by alkali metals. Electron transfer from the surface to the LUMO of CO₂ to form an activated CO₂^{-δ} species is the key step to CO₂ reduction on catalytic surfaces, which was found to be affected by temperature, the presence of promoters, surface morphology and surface defects. Despite these many experimental studies, the energetics of CO₂ reduction over iron surfaces are still not well understood. Although the extent of CO₂ activation has been investigated computationally on various low Miller index surfaces of Cu^{11, 12}, Ni¹³ and Co¹⁴ as well as its dissociation and hydrogenation¹⁵⁻²¹, this is not the case for the Fe facets, where there is no detailed computational study to complement the extensive experimental work²²⁻²⁷.

Under the same experimental conditions, at 300 K, CO₂ activation and dissociation and sequential CO dissociation were reported on Fe (111), but no interaction was observed on the Fe (110) facet²²⁻²⁴. Bent CO₂ as a precursor to dissociation has also been reported between 160-180 K²⁵ and at 130 K²⁶ on Fe (111). Hess et al.²⁶, using high resolution electron loss spectroscopy (HREELS) studies, observed a weakly bound unstable linear CO₂ mode and two stable bent CO₂ modes on the (111) facet. CO₂ dissociation starts at 130 K and CO dissociation at about room temperature. On the (100) facet, Nassir and Dwyer²⁷ first reported the activation of CO₂ on at a slightly lower energy than on the (111) surface and they concluded from their results that both the (111) and (100) surfaces behaved in a similar reactive manner compared to the unreactive (110) facet. Using temperature programmed desorption (TPD) they observed stable C_s and C_{2v} bent CO₂ adsorption modes compared to the linear CO₂ on the surface, two sequential C-O dissociations and a stable CO intermediate, whereas low energy electron diffraction (LEED) analysis indicated the hollow site as the preferred CO₂ adsorption site. Activation was observed on the Fe (100) at 110 K, leading to dissociation at 300K, CO dissociation at 723 K and carbon desorption at 973 K. Recombination of atomic carbon and oxygen of dissociated CO species at

elevated temperatures was also reported at 927 K. These experimental studies and other theoretical studies on Ni, Cu and Co show that apart from the type of metal, CO₂ activation is also affected by the surface morphology.

Earlier theoretical works have reported spontaneous CO₂ activation on the low Miller indices of iron and the energetics to dissociate CO₂ species on the (100) and (111) surfaces but not the (110) surface^{28–33}. A recent DFT study has shown that nickel deposition on iron surfaces increased the work function of the (100) and (111) facets but reduced the work function of the most stable and close-packed (110) surface³⁴. This result suggests that Ni monolayer deposition may affect the thermodynamics and/or kinetics of CO₂ adsorption and dissociation. To understand fully the role of the surface structure and composition on the energetics of CO₂ dissociation on the Ni-deposited Fe surfaces, here we have calculated the adsorption energies, activation energy barriers and geometric structures of reactants, products, and transition states of the process of CO₂ dissociation on bare Fe surfaces and compared them with those on the same surfaces coated in a monolayer of nickel.

2. Computational Details

All calculations were carried out using the generalized gradient approximation (GGA) within the spin-polarized density functional theory (DFT) method with plane-wave basis set and ultra-soft pseudopotentials, as described within the Quantum ESPRESSO Package³⁵, which performs fully self-consistent DFT calculations to solve the Kohn-Sham equations³⁶. The Perdew, Burke, Ernzerhof (PBE)³⁷ GGA exchange-correlation functional was employed. The Fermi-surface effects were treated by the smearing technique of Fermi-Dirac, using a smearing parameter of 0.003 Ry in all calculations. An energy convergence threshold defining self-consistency of the

electron density was set to 10^{-6} eV and a defining mixing factor for self-consistency of 0.2. The graphics of the atomic structures were prepared with the XCrysDen software³⁸.

The various low Miller index surfaces were created from the optimized bulk using the METADISE³⁹ code. Surfaces were described by a slab model, where periodic boundary conditions are applied to the central super-cell so that it is reproduced periodically throughout space. Super-cells large enough to prevent lateral interactions between adsorbates were employed, such that adsorbates (molecular and dissociated species) are more than 5 Å away from their periodic images. Super-cells of the $p(3 \times 3)$ (100) surface, $p(2 \times 2)$ (110) surface and $p(3 \times 2)$ (111) surface were employed for both adsorption and dissociation studies, representing CO₂ surface coverages of 1/9, 1/8 and 1/6 respectively. The surface coverage is defined as the number of adsorbed CO₂ molecules relative to the number of metal atoms in the topmost layer of each surface. The Brillouin zone was sampled using a Monkhorst-Pack⁴⁰ k-point mesh of (9 x 9 x 9) for the bulk material and (3 x 3 x 1), (5 x 5 x 1) and (3 x 5 x 1) mesh k-points for the (100), (110) and (111) surface calculations respectively. A vacuum region of 12 Å perpendicular to each surface was tested to be sufficient to avoid interactions between periodic slabs. An energy cut-off of 40 Ry (544 eV) and charge density cut-off of 320 Ry (4354 eV) for the expansion of the plane-wave basis set were found to be adequate for converging the total energy of the bulk iron to 1 meV.

Following convergence tests, the (110), (100) and (111) slabs were built to thicknesses of 4, 5 and 6 layers, respectively, which settings are sufficient to converge the surface energies of the facets³⁴. The top layer of iron is replaced with nickel in the nickel-deposited surfaces resulting in a total surface coverage. In all calculations, the top 3 layers and adsorbates were allowed to relax

explicitly and the bottom layers were fixed at their bulk equilibrium position to mimic the bulk material. The amount of charge gained by the CO₂ molecule from each surface was calculated using the Löwdin scheme⁴¹. The transition state structures were searched using the climbing image nudged elastic band (CI-NEB) method⁴² and transition state structures were located as the structure with the highest energy along the reaction coordinate, characterised by one and only one imaginary frequency. The reaction energy (ΔE) is calculated as the total energy difference between the final state and the reactants. Energy barriers are also calculated as the total energy difference between the transition state and the reactants. London dispersion interactions were not accounted for in the present study, as recent periodic DFT calculations of the water gas shift reaction on Cu(321) shows that including dispersion terms does not change the qualitative picture of the overall reaction, maintaining both the rate determining step and the predominant route. However, we do expect that the dispersion contributions may make a difference to the stability of the CO₂ molecule, intermediates or products on the different Fe surfaces⁴³.

3. Results and Discussion

3.1 Adsorption sites, modes and strengths of CO₂ on bare and Ni-deposited Fe surfaces

We first explored the preferred CO₂ binding sites (Figure 1) and different modes of binding on the bare Fe (100), (110) and (111) facets and later introduced nickel to the surfaces at the most preferred adsorption modes. The initial adsorption sites investigated included the top, bridge and hollow sites as well as the sub-layer top site (shallow top), the sub-sub-layer top site (deep top) and the sub-layer bridge site (shallow bridge) on the (111) surface, as indicated in Figure 1.

For each adsorption structure, energy minimizations were carried out until convergence within 1 meV per cell was achieved. The lowest-energy CO₂ adsorption structures on the bare and Ni-deposited surfaces are presented in Figures 2 and 3, respectively, (the remaining binding modes

and calculated binding energies are given in the Supporting Information (SI) Figure S1–S3 and Table S1).

For the Fe (100) surface calculations, a $p(3 \times 3)$ super-cell was employed for the CO₂ adsorption and dissociation reactions, similar to earlier calculations^{28,29}. The super-cell is made up of nine surface atoms and five atomic layers. The lowest-energy CO₂ adsorption configuration at the Fe(100) surface was calculated at the hollow site in the C_{2v} mode, where the CO₂ molecule binds through the carbon and two oxygen atoms (Figure 2a), releasing an energy of 88.7 kJmol⁻¹ upon adsorption (Table 1). The adsorption energies of the other stable adsorption configurations are calculated at -62.7 kJmol⁻¹ for CO₂ adsorption at bridge site, -53.7 kJmol⁻¹ for the C_s mode at the hollow site, -15.4 kJmol⁻¹ for CO₂ adsorption at top Fe site, and -2.0 kJmol⁻¹ for linearly physisorbed CO₂. (SI Figure S1b–d). The calculated adsorption energies and structural parameters of the lowest-energy structure are similar to those reported in earlier investigations.^{28,}

²⁹ Glezakou et al.²⁸ also obtained the hollow-C_{2v} structure as the preferred CO₂ activated mode on the Fe (100) surface with an adsorption energy of -69.9 kJmol⁻¹, when they studied CO₂ corrosion pathways using spin-polarized DFT and norm-conserving pseudopotentials. Later, Liu et al.²⁹, employing spin-polarized DFT and projected augmented wave pseudopotentials, also reported the hollow-C_{2v} structure as the preferred structure with an adsorption energy of -61.9 kJmol⁻¹. Recently, Nie et al. have similarly obtained the hollow-C_{2v} structure, with a binding energy of -91.66 kJmol⁻¹ with the DFT-GGA calculation using projected augmented wave pseudopotentials. These results are consistent with our binding energy of -88.7 kJmol⁻¹ at the Fe(100) surface, where the small difference could be attributed to the differences in pseudopotentials employed. On the Ni-deposited Fe(100) surface (Figure 3a), the binding site and mode of CO₂ adsorption remains the same as on the bare Fe(100) surface, but the adsorption

becomes unstable with an endothermic energy of $+47.2 \text{ kJmol}^{-1}$. This drastic change in binding strength from -88.7 kJmol^{-1} to $+47.2 \text{ kJmol}^{-1}$ could at least in part be attributed to the higher electronegativity of nickel, resulting in less electron transfer into the CO_2 moiety, as nickel is observed to bind adsorbates less strongly compared to iron^{13, 30}. For the pure fcc nickel metal, the CO_2 binding energy was calculated to be -7.7 kJmol^{-1} at the Ni (100) surface¹³.

For the CO_2 -Fe(110) complexes, a $p(2 \times 2)$ super-cell made up of eight top atoms and four atomic layers was employed for the CO_2 adsorption and dissociation reactions. As on the Fe(100) surface, several possible sites and modes of adsorption of CO_2 including bridge- C_{2v} , hollow- C_{2v} and hollow- C_s configurations were explored on the Fe(110) surface in order to predict the lowest-energy structure. The hollow- C_s structure (Figure 2b), was calculated to be the preferred CO_2 adsorption mode on the Fe (110) surface, with an adsorption energy of -70.8 kJmol^{-1} . This structure is energetically more stable than the hollow- C_{2v} structure (SI Figure S2b) and the bridge- C_{2v} structure (SI Figure S2c) which released adsorption energies of -46.8 kJmol^{-1} and 45.6 kJmol^{-1} , respectively. The lowest-energy hollow- C_s structure (Figure 2b), was previously reported by Wang et al.³⁰ on Fe (110), where they used a five atomic-layered slab to obtain an adsorption energy of -65.9 kJmol^{-1} (Table 2), consistent with the -70.8 kJmol^{-1} obtained in this work. On the nickel-deposited Fe(110) surface, the CO_2 remains at the preferred hollow site (see Figure 3b), but the binding energy is reduced from -70.8 kJmol^{-1} to -29.5 kJmol^{-1} due to weak interactions between the CO_2 and the interacting Ni atoms, which results in less electron transfer to the adsorbate. Compared to the bare Fe(110) surface, where the CO_2 molecule was adsorbed in 4-fold coordination, at the Ni-covered (110) surface, the CO_2 molecule is 2-fold coordinated to the Ni atoms, which explains the weaker adsorption energy calculated for the Ni-covered surface.

On the Fe(111) surface, a $p(3 \times 2)$ super-cell was employed for both CO₂ adsorption and dissociation. We have explored several initial guess CO₂ structures adsorbed at bridge, shallow top, shallow bridge and deep top adsorption sites in order to determine the lowest-energy structure. Shown in Figure 2c is the lowest-energy CO₂ adsorption structure identified at the Fe(111) surface, the other stable structures calculated are shown in (SI Figure S3). In the lowest-energy bridge-C_{2v} structure (Figure 2c), the carbon atom binds at the shallow top site and the oxygen atoms bind at the top bridge site, releasing an adsorption energy of -116.8 kJmol⁻¹ (see Table 1). Compared to the bridge-C_{2v} structure, positive adsorption energy energies of 27.1 kJmol⁻¹ and 1.7 kJmol⁻¹ were calculated for the top-C_{2v} structure (SI Figure S3a) and the slanted linear CO₂ structure (SI Figure S3b), respectively. The vertical linear structure at the top Fe site (SI Figure S3c) released only small adsorption energy of -1.1 kJmol⁻¹. These adsorption energies suggest that the C_{2v} bent and linear vertical modes are stable CO₂ structures on the surface, as reported in earlier experimental work¹⁰. The bridge-C_{2v} structure was also previously predicted to be the bent adsorption mode of CO₂ at the Fe (111) surface; Ho and co-workers used spin polarised density functional theory to study CO₂ hydrogenation to formate and then its dissociation on Fe (111).^{31, 32} They reported an adsorption energy of -107.1 kJmol⁻¹ for CO₂ adsorption, which compares well with our result of -116.8 kJmol⁻¹. On the Ni-deposited Fe(111) surface, CO₂ remains at the bridge shallow site (see Figure 3c), with the binding strength of CO₂ reduced from -116.8 kJmol⁻¹ to -65.0 kJmol⁻¹ with a reduced amount of charge transfer to the CO₂ moiety.

Generally, CO₂ is more stable in the C_s mode on the close-packed (110) surface, whereas, as also suggested by experiment, the more open (100) and (111) surfaces behave almost alike, with CO₂ adsorbing in the C_{2v} mode. The C_s adsorption mode reduces the coordination number (to two

instead of three) as well as surface interactions and charge transfer between CO₂ and the (110) surface, due to the high surface atom density and crowding at the hollow site on the close-packed (110) face. The trend in the adsorption energies shows that CO₂ adsorption is most favoured on the open and least stable surfaces in the order (111) > (100) > (110), i.e. -116.8 kJmol⁻¹ > -88.7 kJmol⁻¹ > -70.8 kJmol⁻¹. This finding is consistent with the work of O'Shea et al.¹⁴ on cobalt metal surfaces, who observed that CO₂ interacts and binds most strongly to the most open low Miller index (110) surface of fcc Co metal. Ni deposition on the Fe surfaces is found to drastically reduce the adsorption strength of CO₂, with the adsorption even becoming endothermic at the Ni-deposited (100) surface. The observed trend for CO₂ adsorption on the Ni-deposited surfaces is (100) +47.2 kJmol⁻¹ < (110) -29.5 kJmol⁻¹ < (111) -65.0 kJmol⁻¹, with the binding least favoured on Fe(100), where the adsorbed CO₂ interacts primarily with the iron beneath the nickel layer at the hollow site. The molecular binding energies of CO₂ on pure Ni (fcc) were reported to be -7.7 kJmol⁻¹ at Ni (100), -37.6 kJmol⁻¹ at Ni (110) and +29.9 kJmol⁻¹ at Ni (111) surfaces, respectively,¹³ where adsorption is endothermic on one of the surfaces of nickel. The endothermic binding energies of CO₂ on Ni (111) and Ni-doped Fe(100) seem to suggest that the CO₂ moiety prefers to be free rather than bind to these surfaces. The electronic contributions to the observed differences in the reactivity of the bare Fe surfaces to the Ni-deposited surfaces towards CO₂ activation are discussed in the next section.

3.2 Electronic properties and vibrational frequency analyses

The activation of CO₂ was found to be characterized by charge transfer from the iron slab to the activated moiety, where the extent of CO₂ activation, measured from the elongation of the C-O bond, is found to be proportional to the extent of charge transfer. Indeed a plot of the C-O bond distance against the charge gained by the CO₂ adsorbed in the lowest-energy structures at the

different surfaces (Figure 4) shows a linear correlation between the amount of charge transfer and the extent of CO₂ activation. The order of the C-O bond activation is Fe(100) > Fe/Ni(100) > Fe (111) > Fe(110) > Fe/Ni(110) > Fe/Ni(111), which is thus the same as the order for the amount of charge gained by the CO₂ molecule. Compared to the bare Fe surfaces, we observed a smaller degree of charge transfer from the Ni-deposited surfaces to the CO₂, which is consistent with the weaker binding and shorter C-O bonds calculated at the Ni-surfaces than on the bare Fe surfaces.

Although we observed that on a particular facet stronger binding corresponds to more charge transfer, the same cannot be said across the various facets. Whereas we would expect the (111) surface to activate CO₂ to the highest degree, due to its largest CO₂ binding energy, we observed, however, that CO₂ activation is most pronounced on the (100) facet, the surface with the lowest work function. Similarly, Wang et al.³⁰ did not find a strong correlation between CO₂ activation and binding strength across different transition metals (first row TM) and therefore attributed the strength of interaction to both the extent of activation and the *d*-band centre of the metal. We have also observed that for different surface structures of the same material or composition, the binding energy does not correlate to, or does not solely define, the extent of activation. Our study suggests that the extent of activation should be attributed to the extent of electron transfer.

Vibrational analyses of all the adsorption structures yielded no imaginary frequencies, showing that these structures are local minima. Table 2 summarises the three distinct high-frequency vibrational frequencies, which correspond to the symmetric (ν_s) and asymmetric (ν_{as}) stretching modes and the (ν_b) bending mode for CO₂ adsorbed in the most stable adsorption configuration on each surface. For the lowest-energy adsorption structure on the Fe (100) surface (Figure 3a),

the ν_s , ν_{as} , and ν_b modes can be assigned to 846.1 cm^{-1} , 1112.1 cm^{-1} and 750.3 cm^{-1} , respectively. For the most stable adsorption geometry at the Fe (110) surface (Figure 3b), the ν_s , ν_{as} , and ν_b were assigned to 810.3 cm^{-1} , 1505.8 cm^{-1} and 733.5 cm^{-1} . On the Fe (111) surface, the ν_s , ν_{as} , and ν_b modes for the lowest-energy adsorption structure (Figure 3c) can be assigned to 1006.7 cm^{-1} , 1246.4 cm^{-1} and 750.3 cm^{-1} . We note that on all three surfaces there is a significant redshift of the ν_s and ν_{as} modes, compared with the values (1300.0 and 2105.7 cm^{-1}) of a free CO_2 molecule, whereas the bending modes are blue-shifted. The significant red-shifts in the stretching modes show that the CO_2 molecule is activated, which is consistent with the calculated elongated C-O bonds and bent $\angle\text{OCO}$ angles. The C-O stretching vibrational frequencies of CO_2 adsorbed on the deposited surfaces are less red- and blue-shifted compared to the bare Fe surfaces, which indicates lesser CO_2 activation on these nickel-modified surfaces than on the bare Fe surfaces.

3.3 CO_2 dissociation on bare and Ni-deposited Fe surfaces

We next sought to determine the preferred dissociation site of CO_2 ($\text{CO}_2 \rightarrow \text{CO} + \text{O}$). The reaction energy (ΔE) is calculated as the total energy difference between the final state (*i.e.* slab with both $\text{CO} + \text{O}$ adsorbed on it) and the reactants (*i.e.* isolated slab + isolated CO_2). To this end, the inter-nuclear C-O bond distance was increased beyond the C-O bonding distance and the dissociated oxygen atom was placed at various sites on the surface *i.e.* top, bridge and hollow sites (see Figure 1). For each adsorption structure, energy minimizations were carried out until convergence within 1 meV per cell was achieved. Several initial sites were explored on each surface for the dissociated CO and O fragments in order to determine the most stable adsorption sites and structures.

On the bare Fe(100) surface, we found that the hollow site was the preferred adsorption site for both CO and O (see Figure 5a, Table 3). The adsorption of both CO and O at the hollow sites released an adsorption energy of $-179.9 \text{ kJmol}^{-1}$, whereas for the co-adsorption of oxygen at the bridge site with CO at the hollow site, an adsorption energy of $-143.7 \text{ kJmol}^{-1}$ was released. Our results are consistent with those of Glezakov et al., who reported a co-adsorption energy of $-126.0 \text{ kJmol}^{-1}$ for CO and O at the hollow sites using the projected augmented wave pseudopotentials²⁸. On the nickel-deposited Fe(100) surface (Figure 6a), the CO moves from the most table hollow site to the bridge site. The co-adsorption energy released reduced drastically from $-179.9 \text{ kJmol}^{-1}$ to -0.7 kJmol^{-1} , partly due to the change in binding site and weaker binding, as observed even for bare nickel surfaces when compared to bare iron surfaces^{13, 30}. The bridge site shows more affinity for the adsorbate as the electron density is reduced at the hollow site due to an increased gap between nickel atoms (as a result of their smaller size) and higher nickel electronegativity.

On the Fe(110) surface, we found the hollow sites to be the preferred adsorption sites for both CO and O species after geometry optimisations (Figure 5b). The co-adsorption energy was calculated at $-202.4 \text{ kJmol}^{-1}$ as shown in Table 3. Compared to the Fe(100) surface, the CO molecule was adsorbed in an upright configuration at the Fe (110) surface. No stable structure was obtained for O at a top or bridge site, as it moved to the hollow site during energy minimization. On the Ni-deposited Fe(110) surface, the hollow sites remained the preferred binding site for CO and O (Figure 6b), but the co-adsorption energy of (CO + O) reduced from $-202.4 \text{ kJmol}^{-1}$ to $-114.6 \text{ kJmol}^{-1}$. Here again, we see that the nickel reduces the binding strength due to the higher electronegativity of nickel compared to iron. The CO bond is also less

activated, i.e. being 1.19 Å compared to 1.21 Å on the bare surface due to less electron transfer (see Table 3).

On the Fe(111) surface, we found the preferred adsorption sites for both CO and O at the shallow top sites, with an exothermic adsorption energy of $-128.8 \text{ kJmol}^{-1}$ (Figure 5c, Table 3). On the Ni-deposited Fe(111) surface (Figure 6c), the co-adsorption of CO and O was calculated at -52.4 kJmol^{-1} compared to $-128.8 \text{ kJmol}^{-1}$ calculated on the bare Fe(111). On the clean Fe surfaces, we observed that (CO + O) binds most strongly to the facet, where CO₂ binds least strongly, with the (CO + O) binding energies following the trend (110) > (100) > (111). On the Ni-deposited surfaces, the observed trend is (100) < (111) < (110), which suggests that the (CO + O) species bind more strongly to the close-packed (110) surface than the more opened (111) surface. This scenario was also observed on the low Miller index surfaces of nickel¹³, where the Ni (110), the most open facet, binds CO₂ most strongly but only weakly binds CO + O. The molecular and dissociative (CO + O) binding energies of CO₂ were reported at -7.7 and $-116.7 \text{ kJmol}^{-1}$ at Ni (100); -37.6 and -69.5 kJmol^{-1} at Ni (110); $+29.9$ and -51.1 kJmol^{-1} at Ni (111) surfaces, respectively. These results suggest that (CO + O) binds most strongly to the surface with the highest work function, due to the strong affinity of the surface towards electrophiles like oxygen.

3.4 Energy barriers to CO₂ activation and dissociation

Unlike the previous studies of CO₂ dissociation energies on Fe (100)²⁸ and Fe (111)³² that focused on the barriers leading to dissociation, we have calculated both the activation energies required for CO₂ adsorption (activation) and dissociation by locating the transition state structures TS1 and TS2 between the stable states of the isolated, adsorbed and dissociated CO₂

molecule on the various iron facets. The reaction energy profiles for CO₂ dissociation on both the bare Fe and Ni-deposited surfaces is shown in Figure 7, whereas the geometries of stationary point structures along the reaction coordinate are shown in SI Figure S4-S6. All of the reported energies were corrected by the zero-point energy (ΔZPE), calculated as the difference between the zero point vibrational contributions, $\left(\sum_{i=1}^{3n-6} \frac{hv_i}{2} \right)$, of the final adsorbed CO₂ and the initial gaseous CO₂, where h is Plank's constant and v is the vibrational frequency.

It can be seen from the energy profile that the CO₂ dissociation step on the facets is the rate-determining step. The rate depends on the barrier to C-O bond dissociation (**TS2**) and not to adsorption (**TS1**), which is highest on the bare (110) surface. Although the barrier to CO₂ adsorption is rarely explored in the literature, it reveals additional information about the ease of transformation. The negative activation energy barriers (TS1) of -9.8 kJmol⁻¹ and -4.6 kJmol⁻¹ on the Fe(100) and Fe(111) surfaces, respectively, suggest a barrier-less reaction to adsorb and activate CO₂ on these surfaces. However, an energy barrier of 19.6 kJmol⁻¹ has to be overcome to adsorb and activate CO₂ on the Fe(110) surface, indicating that CO₂ will more easily desorb from the Fe(110) surface than continue to dissociation. The energy barriers for dissociation from the activated state on the pure iron surfaces are calculated to be 40.3 kJmol⁻¹, 126.9 kJmol⁻¹ and 83.2 kJmol⁻¹ on the (100), (110) and (111) facets, respectively, with ZPE correction. The earlier reports by Glezakou et al.²⁸ of a dissociation energy barrier on the (100) facet of 47.3 kJmol⁻¹ and Chen et al.³² on the (111) facet of 90.9 kJmol⁻¹ agree well with our calculated values of 46.3 kJmol⁻¹ and 85.6 kJmol⁻¹, respectively, without the zero-point vibrational energy corrections.

On the nickel-deposited surfaces, the barrier to dissociation is lowest on the (100) surface with a barrier of 76.7 kJmol⁻¹, followed by the (110) surface with a barrier of 88.3 kJmol⁻¹, and finally

the (111) surface with barrier of 129.6 kJmol^{-1} . Compared to the bare Fe surfaces, the barriers leading to CO_2 dissociation on the Ni-deposited surfaces increased by 36.4 kJmol^{-1} and 46.4 kJmol^{-1} on the (100) and (111) surfaces, respectively, but decreased by 38.6 kJmol^{-1} on the (110) surface. These results corresponds to the increased work functions calculated at the (100) and (111) facets upon the deposition of a monolayer of nickel. The work functions on the various facets, i.e. the bare Fe(100), Fe(111), Fe(110) and nickel-coated Fe(100), Fe(111) and Fe(110) surfaces have been calculated to be 3.80, 3.86, 4.57, 4.29, 4.28 and 4.72 eV, respectively³⁴. Although the dissociated CO_2 states are lower in energy than the molecularly adsorbed states, the barriers to be overcome in order to desorb CO_2 from the Fe and Ni/Fe surfaces are generally lower than the barriers to dissociate the molecule into CO and O species, suggesting that the adsorbed CO_2 molecule may easily desorb from the surfaces rather than dissociate. On the Ni/Fe (100) and (111) surfaces, the activation energy barriers to dissociation of the CO_2 molecule are even higher than the barriers to desorption, indicating that the activated CO_2 moiety will either remain molecularly adsorbed or desorb from these Ni/Fe surface rather than dissociate. A previous study²⁹ of CO_2 decomposition on (100) surfaces of fcc iron and nickel revealed an increased barrier to dissociation relative to the gaseous CO_2 , while the barrier from the activated to dissociated states showed that dissociation on Ni (100) was faster, with barriers of 51.0 kJmol^{-1} and 113.4 kJmol^{-1} on nickel and iron, respectively, although CO_2 activation was more prominent on the iron facet. As shown in Figure 8, we obtained a correlation between the work function and the activation energies required for CO_2 dissociation, i.e. the higher the work function, the higher the energy barrier to dissociation from its activated state. The regression factor of 0.71 is relatively high and therefore suggests that the work function provides a reasonably accurate indication of the energy requirements for dissociation. The surfaces

exhibiting relatively low work functions are more promising for CO₂ activation and dissociation as they favor electron transfer. However, the observed TS1 barriers indicate that CO₂ dissociation is favoured only on the pure Fe(100) and Fe(111) surfaces, and not on the other surfaces investigated.

We have also plotted the activation energies for the activation and dissociation steps as a function of the reaction energy (Figure 9) and derived the Brønsted-Evans-Polanyi (BET) relationship of the activation and dissociation steps of CO₂ on the Fe and Ni/Fe surfaces. The BEP relationships are important to estimate reaction barriers on other metal surfaces for C–O bond activation and decomposition. As shown in the plot for the activation barriers (ΔE^\ddagger) and the reaction energies for both the activation and decomposition elementary steps for CO₂ dissociation, a linear relationship is obtained, with regression factors of 0.87 and 0.56 respectively. This shows a stronger correlation for the activation step than for the decomposition step, and the BEP relationship has been developed to be $\Delta E^\ddagger = 2.40 \Delta E - 108.03$ (kJmol⁻¹) for CO₂ activation and $\Delta E^\ddagger = 0.71 \Delta E - 153.97$ (kJmol⁻¹) for its dissociation.

4. Summary and Conclusions

CO₂ adsorption and dissociation was investigated on the low-index (100), (110) and (111) surfaces of bcc Fe as well as their facets coated with a monolayer of Ni, using density functional theory calculations within the generalized gradient approximation (GGA-PBE) and exchange correlation functional. We have observed that the adsorption energy for CO₂ decreases in the order Fe (111) > Fe (100) > Fe (110) on the clean surfaces, which is consistent with previous studies. However, we have found that the co-adsorption energies of the dissociated products (CO and O) decrease in the reverse order: Fe (110) > Fe (100) > Fe (111). Nickel deposition favours CO₂ adsorption in the order (111) > (110) > (100) and (CO + O) adsorption in the reverse order,

except on the (100) facet where binding of adsorbates is not favoured. With the calculated energy barriers, the Brønsted-Evans-Polanyi (BEP) relationship was developed with the kinetic energy barriers and reaction energies for both CO₂ activation and dissociation reaction steps. The energy barriers for dissociation of the CO₂ molecule into CO and O species were found to be generally higher than the energy barriers for the activation of the CO₂ molecule. The kinetic energy barriers leading to dissociated CO₂ products on the (100), (110) and (111) surfaces from the activated intermediate were calculated at 40.3 kJmol⁻¹, 126.9 kJmol⁻¹ and 83.2 kJmol⁻¹, respectively, which increases on (100) and (111) and reduces on (110) upon deposition of Ni, as shown in their work function alterations, with changes most pronounced on (111) > (100) > (110). The transition state barriers leading to activation and dissociation show that the CO₂ will prefer to desorb from the Fe (110) facet rather than form surface-bound dissociated species, in good agreement with experimental results, where at 300 K no CO₂ decomposition was observed on the (110) surface compared to the (111) and (100) surfaces. Deposition of a monolayer of Ni on the Fe (110) facet reduces the rate-determining barriers leading to CO₂ dissociation, but generally the unstable activated CO₂ on the various facets will desorb rather than dissociate. The zero point vibrational energy contributions were treated and the energy changes fell within a range of 6.9 to 62 kJmol⁻¹. The direct dissociation process is thermodynamically most favoured on the (110) facet before and after Ni deposition, considering that the activated intermediate is less stable and the dissociated product is most stable on this facet, thus favouring product formation. Thus, at high temperatures CO₂ dissociation to CO and O should be most favourable on the (110) facets. However, despite variations in the work functions of the iron facets upon Ni deposition, suggesting easier decomposition on the (110) but not on the (100) and (111) surfaces, CO₂ decomposition is kinetically challenging on the Ni-doped surfaces, due to the instability of

the activated CO₂ moiety. These findings indicate that, although reducing the work functions of iron surfaces through deposition of a second metal could enhance the kinetics of the direct dissociation of CO₂, especially on the most stable and therefore possibly dominant Fe (110) facet, the thermodynamics remain challenging for CO₂ decomposition, probably resulting in CO₂ desorption from the nickel-doped iron surfaces before dissociation of the molecule into surface-bound species.

Acknowledgements

The authors gratefully acknowledge the UK's Royal Society and the Leverhulme Trust for a research grant under the Royal Society-Leverhulme Africa Award Scheme. EA, RT and CRK acknowledge the National Council for Tertiary Education, Ghana, for a TALIF research grant. NHdL acknowledges the Royal Society for an Industry Fellowship.

References

- (1) H. Arakawa, M. Aresta, J. N. Armor, M. A. Barteau, E. J. Beckman, A. T. Bell, J. E. Bercaw, C. Creutz, E. Dinjus and D. A. Dixon, *Chem. Rev.*, 2001, **101**, 953–996.
- (2) W. Wang, S. Wang, X. Ma and J. Gong, *Chem. Soc. Rev.*, 2011, **40**, 3703–3727.
- (3) J. Ma, N. Sun, X. Zhang, N. Zhao, F. Xiao, W. Wei and Y. A. Sun, *Catal. Today*, 2009, **148**, 221–231.
- (4) S. C. Talmage and C. J. Gobler, *Proc. Natl. Acad. Sci. U. S. A.*, 2010, **107**, 17246–17251.
- (5) G. Centi and S. Perathoner, *Catal. Today*, 2009, **148**, 191–205.
- (6) A. Roldan, N. Hollingsworth, A. Roffey, H.-U. Islam, J.B.M. Goodall, C.R.A. Catlow, J. A. Darr, W. Bras, G. Sankar, K. B. Holt, G. Hogarth and N. H. de Leeuw, *Chem. Commun.*, 2015, **51**, 7501–7504.
- (7) W. Gong, B. Hao, Z. Wei, D. J. Ferguson, T. Tallant, J. A. Krzycki and M. K. Chan, *Proc. Natl. Acad. Sci. U. S. A.*, 2008, **105**, 9558–9563.
- (8) J.-H. Jeoung and H. Dobbek, *Sci.*, 2007, **318**, 1461–1464.
- (9) F. Solymosi, *J. Mol. Catal.*, 1991, **65**, 337–358.
- (10) H.-J. Freund and M. W. Roberts, *Surf. Sci. Rep.*, 1996, **25**, 225–273.
- (11) G.-C. Wang, L. Jiang, Y. Morikawa, J. Nakamura, Z.-S. Cai, Y.-M. Pan and X.-Z. Zhao, *Surf. Sci.*, 2004, **570**, 205–217.
- (12) C. Au and M. Chen, *Chem. Phys. Lett.*, 1997, **4**, 238–244.
- (13) S.-G. Wang, D.-B. Cao, Y.-W. Li, J. Wang and H. Jiao, *J. Phys. Chem. B*, 2005, **109**, 18956–18963.
- (14) V. A. de la Peña O’Shea, S. González, F. Illas, J. L. G. Fierro, *Chem. Phys. Lett.*, 2008, **454**, 262–268.
- (15) P. Bothra, G. Periyasamy and S. K. Pati, *Phys. Chem. Chem. Phys.*, 2013, **15**, 5701–5706.
- (16) D.-B. Cao, Y.-W. Li, J. Wang and H. Jiao, *Surf. Sci.*, 2009, **603**, 2991–2998.
- (17) X. Ding, V. Pagan, M. Peressi and F. Ancilotto, *Mater. Sci. Eng. C*, 2007, **27**, 1355–1359.
- (18) C. Dri, A. Peronio, E. Vesselli, C. Africh, M. Rizzi, A. Baldereschi, M. Peressi and G. Comelli, *Phys. Rev. B*, 2010, **82**, 165403.
- (19) A. A. Peterson, F. Abild-Pedersen, F. Studt, J. Rossmeisl and J. K. Nørskov, *Energy Environ. Sci.*, 2010, **3**, 1311–1315.

- (20) E. Vesselli, M. Rizzi, L. De Rogatis, X. Ding, A. Baraldi, G. Comelli, L. Savio, L. Vattuone, M. Rocca and P. Fornasiero, *J. Phys. Chem. Lett.*, 2010, **1**, 402–406.
- (21) E. Vesselli, L. De Rogatis, X. Ding, A. Baraldi, L. Savio, L. Vattuone, M. Rocca, P. Fornasiero, M. Peressi and A. Baldereschi, *J. Am. Chem. Soc.*, 2008, **130**, 11417–11422.
- (22) K. Yoshida and G. A. Somorjai, *Surf. Sci.*, 1978, **75**, 46–60.
- (23) H. Behner, W. Spiess, G. Wedler and D. Borgmann, *Surf. Sci.*, 1986, **175**, 276–286.
- (24) R. Bauer, *J. Vac. Sci. Technol. A Vacuum, Surfaces, Film*, 1987, **5**, 1110.
- (25) H.-J. Freund, H. Behner, B. Bartos, G. Wedler, H. Kuhlenbeck and M. Neumann, *Surf. Sci.*, 1987, **180**, 550–564.
- (26) G. Hess, H. Froitzheim and C. Baumgartner, *Surf. Sci.*, 1995, **331–333**, 138–143.
- (27) M. H. Nassir, *J. Vac. Sci. Technol. A Vacuum, Surfaces, Film*, 1993, **11**, 2104–2109.
- (28) V.-A. Glezakou, L. X. Dang and B. P. McGrail, *J. Phys. Chem. C*, 2009, **113**, 3691–3696.
- (29) C. Liu, T. R. Cundari and A. K. Wilson, *J. Phys. Chem. C*, 2012, **116**, 5681–5688.
- (30) S.-G. Wang, X.-Y. Liao, D.-B. Cao, C.-F. Huo, Y.-W. Li, J. Wang and H. Jiao, *J. Phys. Chem. C*, 2007, **111**, 16934–16940.
- (31) H.-J. Li and J.-J. Ho, *J. Phys. Chem. C*, 2010, **114**, 1194–1200.
- (32) H.-L. Chen, H.-T. Chen and J.-J. Ho, *Langmuir*, 2010, **26**, 775–781.
- (33) X. Nie, H. Wang, M. J. Janik, X. Guo and C. Song, *J. Phys. Chem. C*, 2016, **120**, 9364–9373.
- (34) C. R. Kwawu, R. Tia, E. Adei, N. Y. Dzade, C. R. A. Catlow and N. H. de Leeuw, *Appl. Surf. Sci.*, 2017, **400**, 293–303.
- (35) P. Giannozzi, S. Baroni, N. Bonini, M. Calandra, R. Car, C. Cavazzoni, D. Ceresoli, G. L. Chiarotti, M. Cococcioni and I. Dabo, *J. Phys. Condens. Matter*, 2009, **21**, 395502.
- (36) W. Kohn and L. J. Sham, *Phys. Rev.*, 1965, **140** (4A).
- (37) J. Perdew, K. Burke and M. Ernzerhof, *Phys. Rev. Lett.*, 1996, **77**, 3865–3868.
- (38) A. Kokalj, *J. Mol. Graph. Model*, 1999, **17**, 176–179.
- (39) G. W. Watson, E. T. Kelsey, N. H. de Leeuw, D. J. Harris and S. C. Parker, *J. Chem. Soc., Faraday Trans.*, 1996, **92**, 433.
- (40) J. D. Pack and H. J. Monkhorst, *Phys. Rev. B*, 1977, **16**, 1748–1749.

- (41) P-O. Löwdin, J. Chem. Phys., 1950, **3**, 18.
- (42) G. Henkelman, B. P. Uberuaga and H. A. Jönsson, J. Chem. Phys., 2000, **113**, 22.
- (43) H. Prats, P. Gamallo, R. Sayós and F. Illas, Phys. Chem. Chem. Phys., 2016,**18**, 2792-2801

LIST OF TABLES

Table 1: Adsorption energy and structural parameters of CO₂ adsorbed on Fe (100), (110) and (111) surfaces.

Surface	Structure	E _{ads} /kJmol ⁻¹	C–O(1), C–O(2) /Å	O–C–O /°	Fe–C /Å	Fe–O(1), Fe–O(2) /Å	Σq /e
Fe(100)	Bare Fe (hollow-C _{2v})	-88.7	1.35	119.29	2.15	2.08	-0.08
	Ni-covered (hollow-C _{2v})	47.2	1.32	121.4	2.10	2.12	-0.07
	Glezakou et al. ²⁸	-69.9	1.35	117.8	2.11	2.08, 2.05	-
Fe(110)	Bare Fe (hollow-C _s)	-70.8	1.36,1.23	126.98	1.98	2.04,2.53	-0.06
	Ni-covered (hollow-C _s)	-29.5	1.29,1.24	132.2	1.98	2.08,2.23	-0.05
	Wang et al. ³⁰	-65.9	1.35, 1.22	128.00	1.96	2.01	-
Fe(111)	Bare Fe (bridge-C _{2v})	-116.8	1.30	122.3	1.98	1.96	-0.06
	Ni-covered (bridge-C _{2v})	-65.0	1.27	127.8	1.90	1.98,1.97	-0.045
	Li and Ho ³¹	-107.1	1.29	122.3	1.96	1.96	-

Table 2: The symmetric (ν_s), asymmetric (ν_{as}) and bending (ν_b) vibrational frequencies of CO₂ adsorbed on the low-miller index Fe surfaces.

Vib. mode	Linear CO ₂	Fe(100)	Fe/Ni(100)	Fe(110)	Fe/Ni(110)	Fe(111)	Fe/Ni(111)
ν_s / cm^{-1}	1300.0 (1351.2) ¹⁰	846.1	923.5	810.3	940.6	1006.7	1078.4
$\nu_{as} / \text{cm}^{-1}$	2105.7 (2396.4) ¹⁰	1112.1	1112.4	1505.8	1506.0	1246.4	1436.3
ν_b / cm^{-1}	700.0 (672.2) ¹⁰	750.3	748.2	733.5	730.5	750.3	739.0

Table 3: Co-adsorption energies and structural parameters of CO + O on Fe (100), (110) and (111) surfaces.

Surface	Nature	O-binding site	CO-binding site	$E_{\text{ads}}/\text{kJmol}^{-1}$	C-O(1) /Å	C-O(2) /Å	Fe-CO /Å	Fe-O /Å
Fe (100)	Bare Fe	hollow	hollow	-179.9	1.31	3.02	2.10	2.10
	Ni-doped	hollow	bridge	-0.7	1.18	3.91	1.90	2.01
Fe (110)	Bare Fe	hollow	hollow	-202.4	1.21	3.97	1.97	1.85
	Ni-doped	hollow	hollow	-114.6	1.19	4.65	1.94	1.87
Fe (111)	Bare Fe	Shallow top	Shallow top	-128.8	1.20	3.90	1.78	1.88
	Ni-doped	Shallow bridge	Shallow bridge	-52.4	1.19	3.01	1.84	1.84

LIST OF FIGURES

Figure 1: Top, bridge and hollow starting adsorption sites on the Fe (100), (110) and (111) facets.

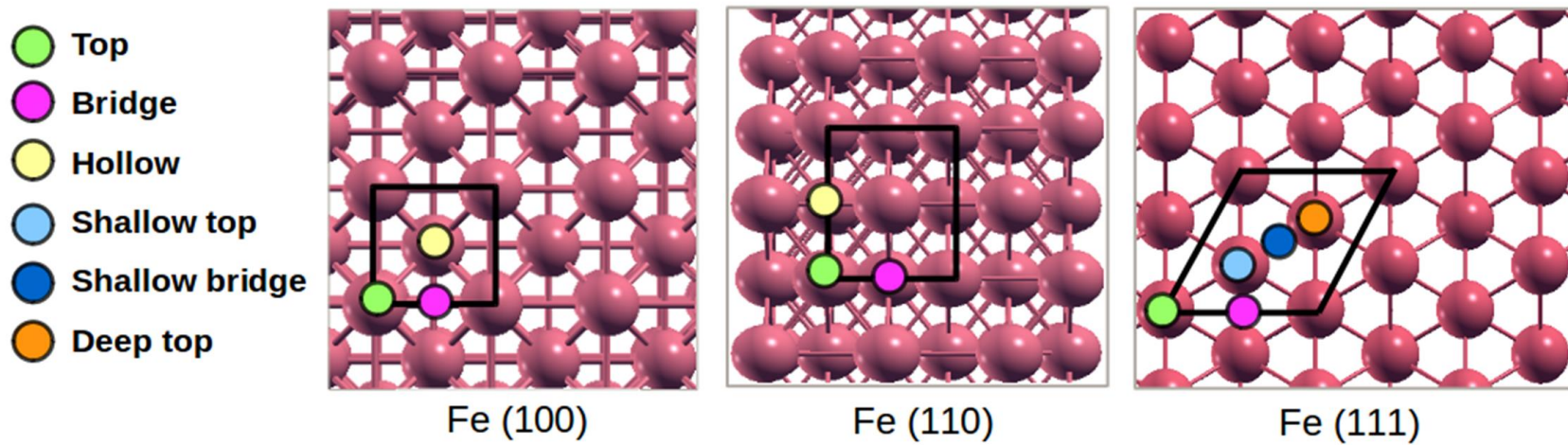
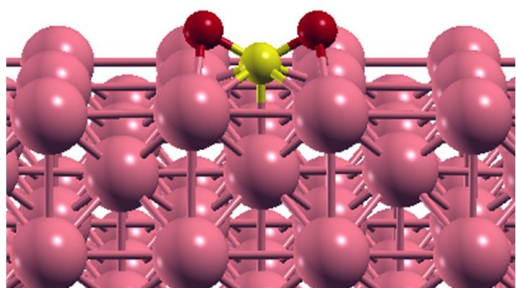


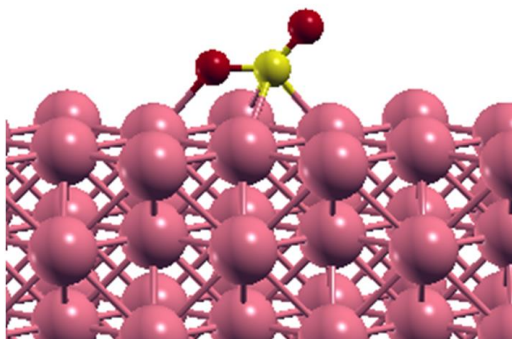
Figure 2: Stable CO₂ adsorption modes on the Fe (100), (110), and (111) surfaces. Colour code: Fe = pink, C = yellow and O = red.

(a) Fe(100)



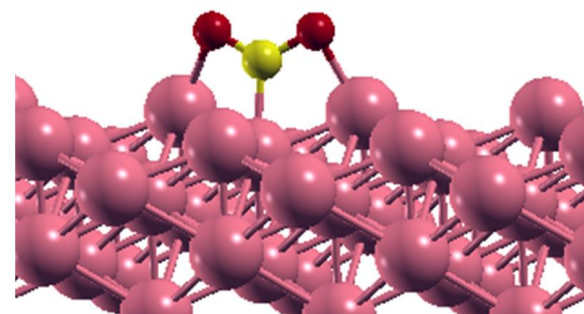
$$E_{\text{ads}} = -88.7 \text{ kJmol}^{-1}$$

(b) Fe(110)



$$E_{\text{ads}} = -70.8 \text{ kJmol}^{-1}$$

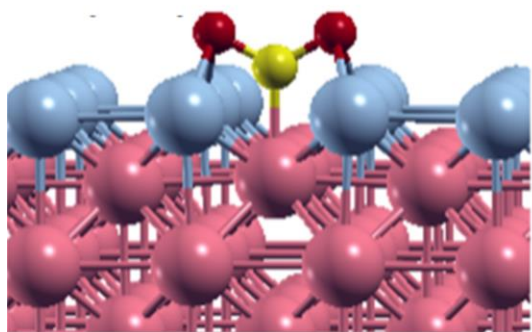
(c) Fe(111)



$$E_{\text{ads}} = -116.8 \text{ kJmol}^{-1}$$

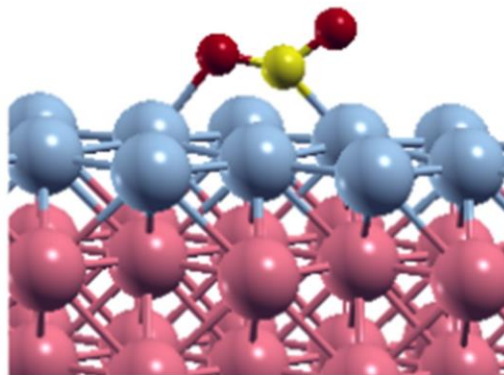
Figure 3: Preferred CO₂ adsorption site on the nickel monolayer covered Fe (100), (110) and (111) surfaces. Colour code: Fe = pink, Ni = blue, C = yellow, and O = red.

(a) Fe(100)



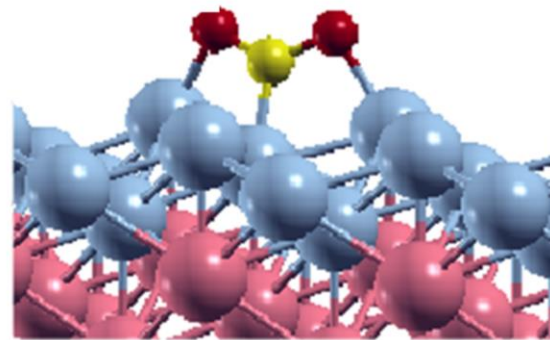
$$E_{\text{ads}} = +47.2 \text{ kJmol}^{-1}$$

(b) Fe(110)



$$E_{\text{ads}} = -29.5 \text{ kJmol}^{-1}$$

(c) Fe(111)



$$E_{\text{ads}} = -65.0 \text{ kJmol}^{-1}$$

Figure 4: Amount of charge gained by CO₂ and the extent of C–O activation.

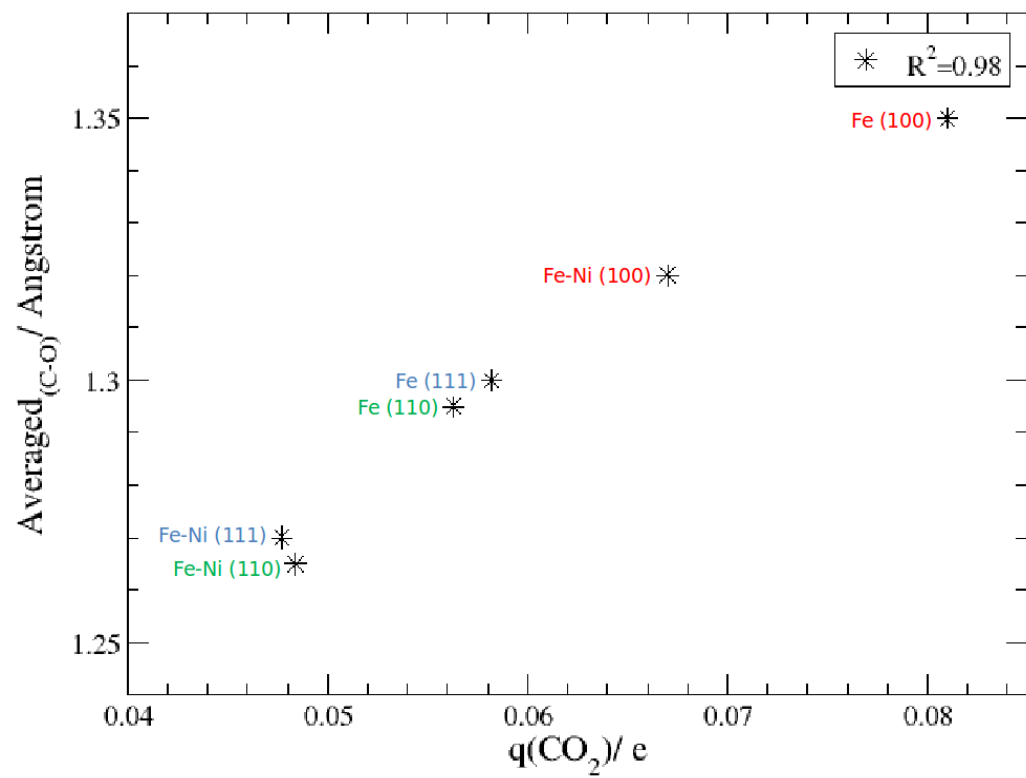
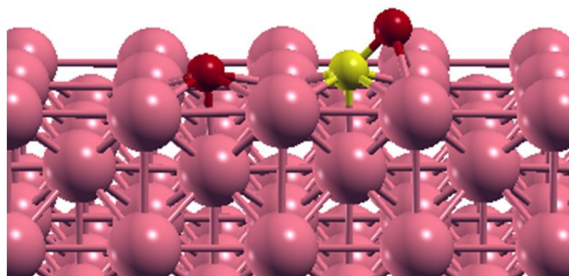


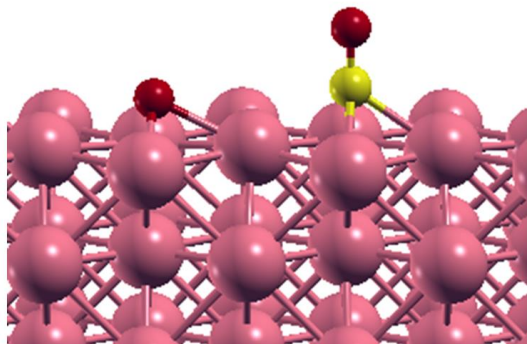
Figure 5: Co-adsorption structures of CO + O s on the Fe (100), (110) and (111) surfaces.

(a) Fe(100)



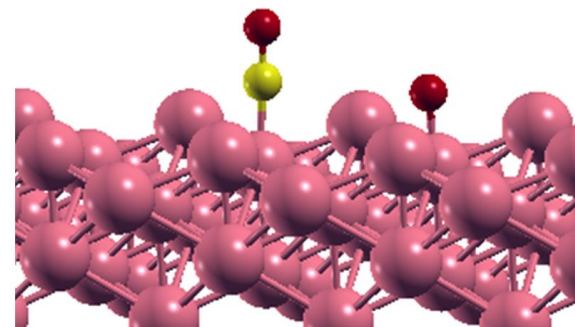
$$E_{\text{ads}} = -179.9 \text{ kJmol}^{-1}$$

(b) Fe(110)



$$E_{\text{ads}} = -202.4 \text{ kJmol}^{-1}$$

(c) Fe(111)



$$E_{\text{ads}} = -128.8 \text{ kJmol}^{-1}$$

Figure 6: CO + O initial and final adsorption modes on the nickel monolayer covered Fe (100), (110) and (111) surfaces.

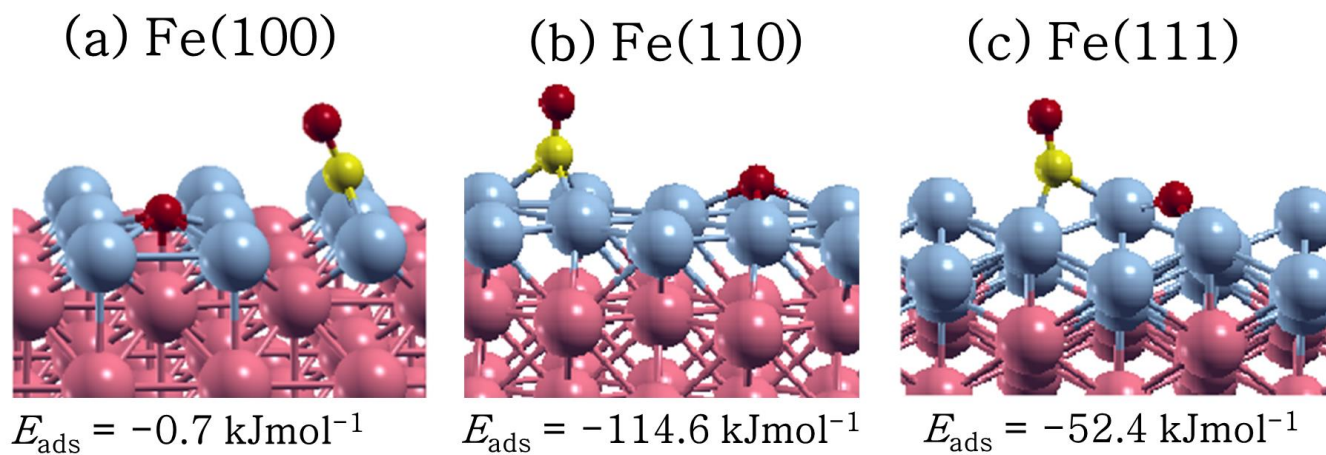


Figure 7 Energy profile diagram for CO₂ activation and dissociation on the bare and Ni-doped Fe (100), (110) and (111) facets, with all energies corrected by the ZPE contribution.

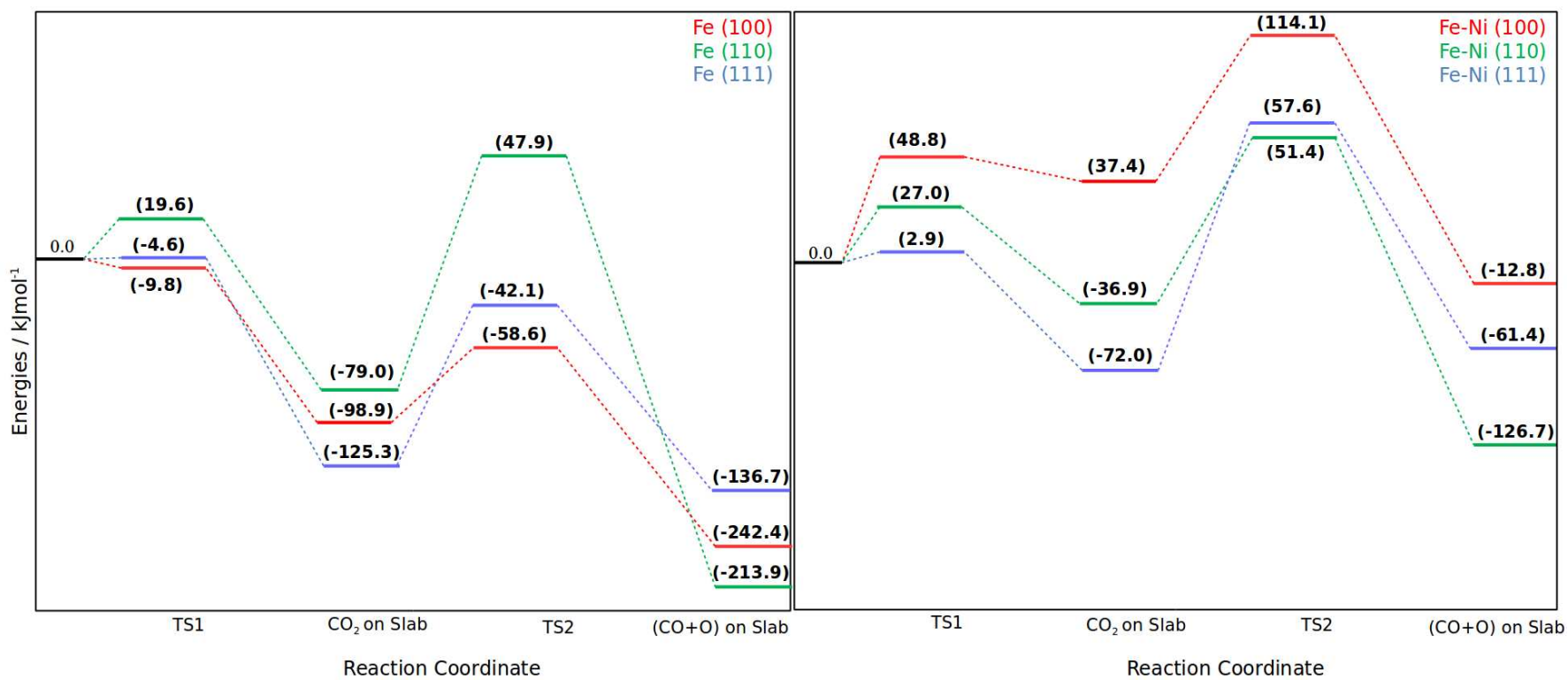


Figure 8: Plot of work functions of Fe and Fe-Ni (100), (110) and (111) facets against kinetic energy barriers.

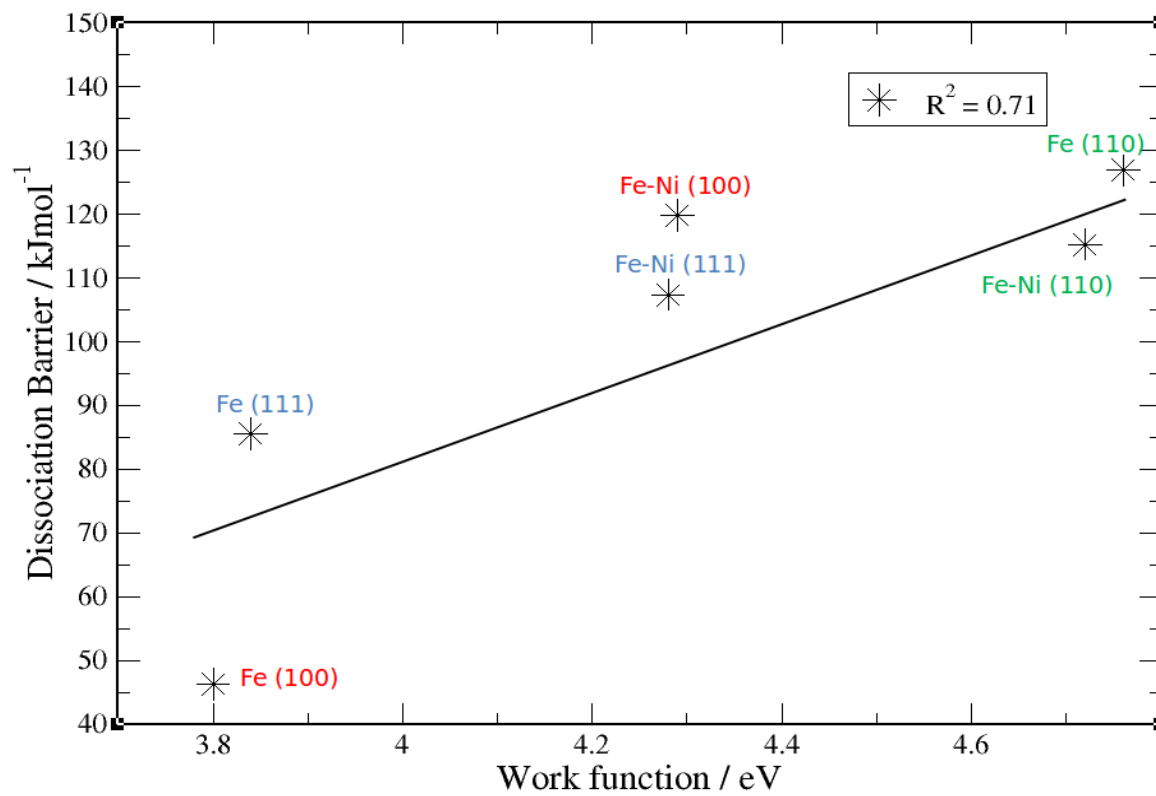


Figure 9: The Brønsted-Evans-Polanyi (BET) Relation; A Plot of Activation Energies against Reaction Energies on bare and Ni-doped Fe(100), (110) and (111) facets.

